Sustainable Marine Structures
https://journals.nasspublishing.com/sms

ARTICLE

Ultimate Capacity of Metal Matrix Composites Sandwich under Impulsive Loads for Marine Structural Applications

Rasgianti [1*] ***, Aldi Fahli Muzaqih*** [2] ***, Ristiyanto Adiputra*** [3*] ***, Ariyana Dwiputra Nugraha*** [1] ***, Almas Aprilana*** [1] ***, Aditya Rio Prabowo*** [2]

[1] *Power Generation System Research Department, PT PLN (Persero) Research Institute, Jakarta 12760, Indonesia*
[2] *Department of Mechanical Engineering, Universitas Sebelas Maret, Surakarta 57126, Indonesia*
[3] *Research Center for Hydrodynamics Technology, National Research and Innovation Agency (BRIN), Surabaya 60112, Indonesia*

ABSTRACT

The growing utilization of the ocean as a renewable energy source drives the need for reliable maritime infrastructure. One major challenge for these structures is withstanding impulsive loads from extreme ocean waves, which requires materials with high strength and deformation resistance to maintain structural integrity. Metal Matrix Composite (MMC) is a promising material, yet studies on its behavior under impulsive loading remain limited. This study investigates the ultimate capacity of MMC sandwich structures using the Finite Element Method (FEM) through simulations with an Underwater Shock Loading Simulator (USLS). Validation against the results of He et al. confirms the accuracy of the simulation method. Results indicate that increasing flyer velocity from 135 to 195 m/s raises the maximum displacement from 5.83 mm to 10.7 mm. Increasing face sheet thickness from 0.4 to 1.8 mm reduces deformation from 4.95 to 3.09 mm, while increasing core thickness from 14 to 20 mm decreases deflection from 5.42 to 3.68 mm. Furthermore, the thickness ratio analysis indicates that the 1:10 configuration produces the smallest deformation (4.13 mm) and is more efficient because it provides higher stiffness with lower

*CORRESPONDING AUTHOR:
Rasgianti, Power Generation System Research Department, PT PLN (Persero) Research Institute, Jakarta 12760, Indonesia; Email: rasgianti1@pln.co.id; Ristianto Adiputra, Research Center for Hydrodynamics Technology, National Research and Innovation Agency (BRIN), Surabaya 60112, Indonesia; Email: Ristiyanto.adiputra@brin.go.id

ARTICLE INFO
Received: 13 October 2025 | Revised: 31 October 2025 | Accepted: 27 November 2025 | Published Online: 10 December 2025
DOI: https://doi.org/10.36956/sms.v7i4.2830

CITATION
Rasgianti, Mzaqih, A.F., Adiputra, R., et al., 2025. Ultimate Capacity of Metal Matrix Composites Sandwich under Impulsive Loads for Marine Structural Applications. Sustainable Marine Structures. 7(4): 168–192. DOI: https://doi.org/10.36956/sms.v7i4.2830

mass. These findings demonstrate that optimizing core and face sheet thickness significantly enhances structural resistance to deformation. The study concludes that a balanced thickness configuration is key to improving the structural performance of MMC sandwiches, supporting the design of stronger and more sustainable materials for maritime structures in extreme environments.

Keywords: Impulsive Load; Marine Structure; Metal Matrix Composite; Sandwich Composite

1. Introduction

Maritime infrastructure development continues to progress in line with the increasing utilization of marine areas [1–3]. The primary challenge of maritime infrastructure is the durability of structures against extreme ocean conditions, particularly high waves that can cause significant damage [4,5]. Support structures in marine environments must be designed to withstand static and dynamic loads, including impulsive loads characterized by high-intensity forces over very short durations [6]. In this context, material selection plays a crucial role, as unsuitable materials not only increase the risk of damage but also affect the service life of the infrastructure [7–9]. One promising material for maritime applications is Metal Matrix Composites (MMC), which offer superior mechanical, thermal, and corrosion properties compared to conventional materials [10,11]. The use of MMC as the core in sandwich structures offers great potential for enhancing specific strength, toughness, and energy absorption capacity under impulsive loads, such as blast waves or impacts [12,13]. To ensure the resilience and reliability of maritime structures, materials must be tested against impulsive loads to adapt to extreme operational conditions while supporting the sustainable development in the marine sector [14,15].

Previous research on testing the strength of Metal Matrix Composite (MMC) materials has been conducted by various researchers with diverse focuses. Marx and Rabiei [16] tested the maximum strength of Steel-Steel Composite Metal Foam (SS-CMF) and Composite Metal Foam Core Sandwich Panels (SS-CMF-CSP) under static loads experimentally. Zhao et al. [17] investigated the strength of sandwich panels with aluminium foam cores under impact loads through material perforation. Latour et al. [18] tested the strength of composite sandwich panels with steel face sheets and aluminium foam cores under bending loads. Styles et al. [19] tested aluminium foam cores under bending loads and studied the effect of core thickness in four-point bending tests. For materials subjected to impulsive loads, Ren et al. [20] analyzed the strength of carbon/epoxy sandwich structures with PVC foam cores under impulsive loads in water experimentally, showing that increased impulsive loads caused permanent deformation. Similar research was conducted by Cui et al. [21], who studied aluminium-based metal sandwich materials under impulsive loads. Avachat and Zhou [22] performed experiments and numerical simulations using a Coupled Eulerian-Lagrangian approach to test hybrid composite materials, demonstrating their superior performance under blast loads. Additionally, Avachart et al. [23] investigated the effects of geometry and size on the strength of composite materials. Zhu et al. [24] analyzed the energy absorption of sandwich panels with aluminium foam cores under blast loads through experiments and Finite Element Method-based simulations. He et al. [25] analyzed the strength of MMC sandwich structures with aluminium face sheets and aluminium foam cores, identifying maximum strength based on the maximum deflection of the test specimens.

Although previous research has provided valuable insights into the static, bending, and impact behavior of sandwich materials. However, existing studies predominantly focus on specific impulsive loading scenarios, leaving limited insights into comprehensive deformation mechanisms under varied loads. There remains a research gap in comprehensively understanding the ultimate strength and deformation behavior of MMC sandwich panels under varying impulsive loads, especially in marine-relevant environments. To address this gap, this study aims to investigate the ultimate capacity and dynamic response of aluminium-based MMC sandwich structures under different impulsive loading conditions.

Moreover, the study highlights the influence of face sheet and core thickness, as these two parameters directly affect deformation[26], structural durability, stability, and the material's ability to absorb high-intensity stresses, which determines the reliability of the structure under extreme conditions[27]. To achieve these objectives, this study will use Finite Element Method (FEM) simulations with a Coupled Eulerian-Lagrangian (CEL) approach in Abaqus Simulia software, which is capable of simulating underwater explosions and evaluating the strength of MMC materials under impulsive loads. The study is expected to contribute to the development of advanced materials that are more robust and reliable for modern maritime technology applications.

2. Methodology

2.1. Flowchart

This study employs the finite element method (FEM) using ABAQUS CAE software to simulate the effects of underwater shock loading. The study began with a literature review, followed by the development of an Underwater Shock Loading Simulator (USLS) model to simulate underwater shock waves. The model comprises the projectile, piston, water tank, flange, test specimen, and fluid domain, each assigned specific material properties. The geometry is then discretized into smaller elements through a meshing process. After that, boundary conditions, loads, geometric interactions, simulation time, and output parameters are defined in the step phase. Initial validation is conducted to ensure the simulation model operates as intended.

A mesh convergence study was performed to determine the optimal mesh size, ensuring accurate and efficient simulations. Once the ideal mesh is established, simulations are carried out with variations in the thickness of the test specimen. The results are evaluated based on the displacement at the specimen's midpoint, which serves as a key metric for its load resistance capability. The overall research methodology is summarized in the flowchart presented in **Figure 1**.

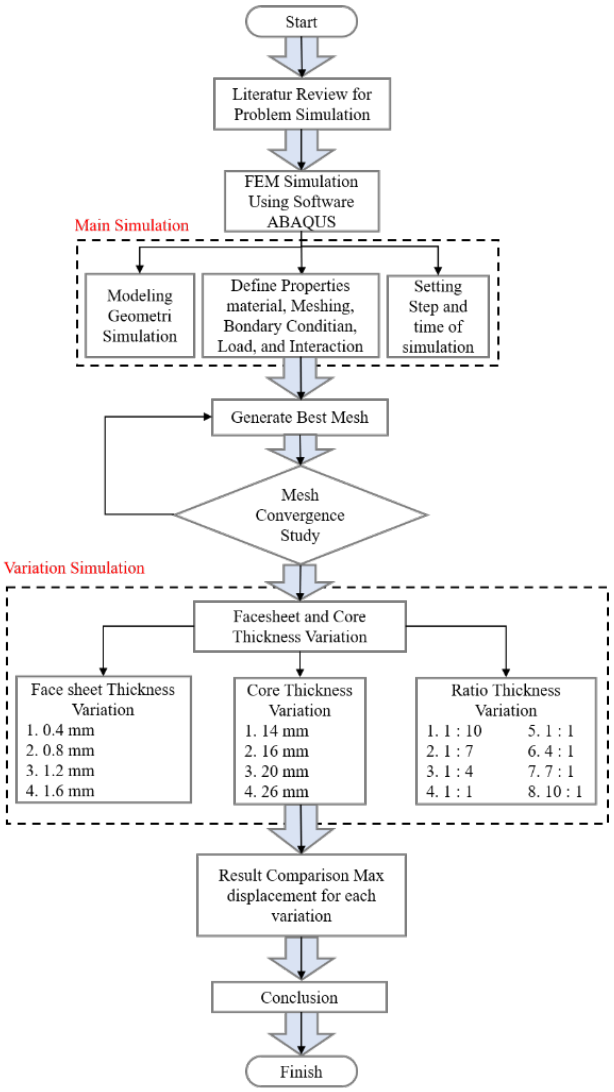

Figure 1. Flowchart FEM model main and variation simulation.

2.2. Model Geometry

The geometric configuration of the Underwater Shock Loading Simulator (USLS) in this study is developed based on the actual experimental apparatus designed by He et al.[25]. The reference model, shown in **Figure 2**, represents a real testing device used to generate underwater shock loading through high-velocity projectile impact. To replicate the physical test conditions, the same geometric dimensions and structural configuration were adopted for the present simulation. The model is reconstructed in three dimensions within ABAQUS/CAE to perform finite element analysis (FEM).

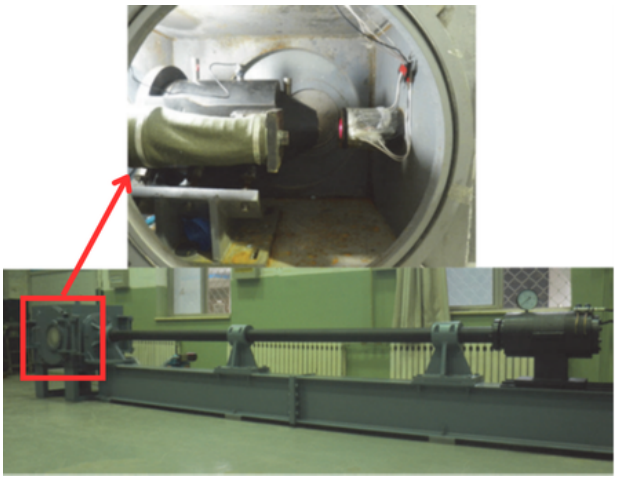

Figure 2. Underwater shock loading experiment device[25].

The USLS consists of a projectile, piston, or flyer, a water tank, flange, test specimen, and surrounding fluid domain. As shown in **Figure 3a,** the water tank includes a front cylindrical chamber and a rear cavity connected through a taper section with an angle of 7°. The diameters of the front and rear chambers are 66 mm and 152.4 mm, respectively, while the total outer diameter of the tank is 292 mm. The cylindrical section, with a length of 76 mm, serves to guide the pressure wave uniformly toward the specimen surface.

Three holes are provided along the tank wall for pressure sensors that record the transient pressure distribution inside the fluid domain. Sensor A is positioned at the front of the chamber with a diameter of 66 mm, Sensor B at 106 mm, and Sensor C at 142 mm. These sensor locations are kept the same in the numerical model to match the measurement points used in the reference experiment. A summary of the USLS geometry dimensions is presented in **Table 1**.

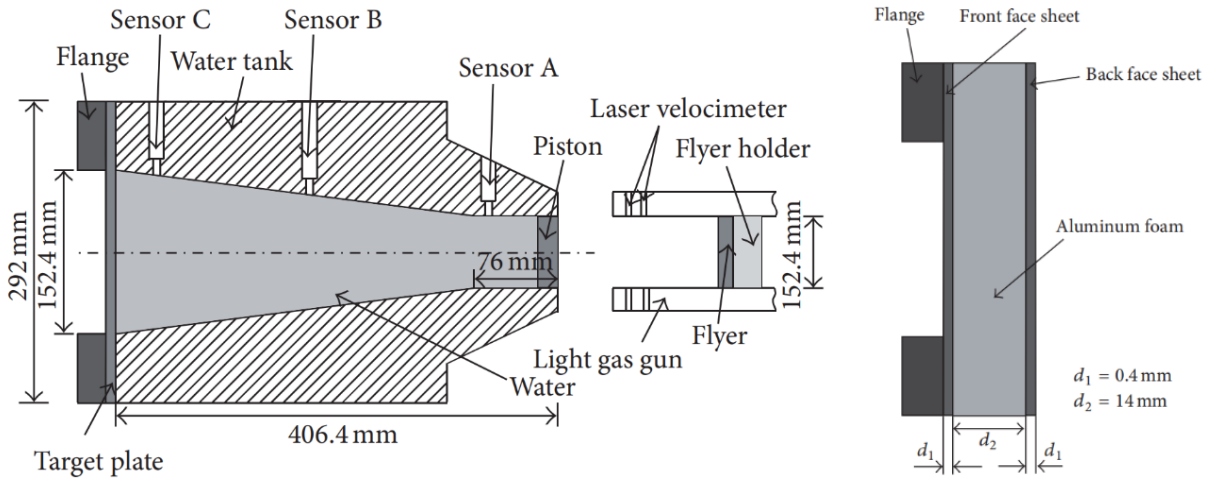

Figure 3. Schematic diagram of: (**a**) USLS; (**b**) Specimen testing[25].

Table 1. Dimension model geometry.

Part	Specification/Dimension
Water Chamber	Front Ø 66 mm; Rear Ø 152.4 mm; Taper Angle 7°
Water tank	Outer Ø 292 mm; Length 406.4 mm
Sensor A Position	At Ø 66 mm
Sensor B Position	At Ø 106 mm
Sensor C Position	At Ø 142 mm
Flange	Thickness: 25.4 mm

The test specimen, shown in **Figure 3b**, is modeled as a circular sandwich panel clamped at its edges by a 25.4 mm thick steel flange made of 42CrMo alloy. This constraint replicates the experimental clamping condition during testing to ensure realistic load transfer. All components of the USLS are subsequently discretized into finite elements, with finer mesh refinement applied around the specimen and the fluid–structure interface to

ensure numerical stability and accuracy during the FEM simulation.

2.3. Material Properties

The materials used in this simulation include the test specimen, projectile, water tank, flange, and the surrounding fluid domain. The test specimen is a metal matrix composite (MMC) consisting of face and back sheets made of 3004 aluminum and a core made of aluminum foam, with their mechanical and physical properties summarized in **Table 2.** The face sheets were modeled using the Johnson–Cook constitutive model due to its ability to capture strain-rate sensitivity and strain hardening under dynamic loading. In this model, the material is assumed to be homogeneous and isotropic, so microstructural details are not explicitly included. The aluminum foam core was represented using a crushable foam model with volumetric hardening. The interface between the face sheet and core was assumed to be perfectly bonded without slip or delamination, allowing the global structural response to be evaluated consistently without interlayer variability.

The structural components of the USLS, including the water tank and flange, were modeled using Steel 4340 (40CrNiMoA), while the piston and projectile were assigned Steel 4140 (30CrMo), with their mechanical properties listed in **Table 3**. Both materials were treated as linear elastic to maintain numerical stability.

The fluid domain was modeled using the Mie–Grüneisen equation of state (EOS) to represent pressure-wave propagation during the impulsive event. The fluid was assumed to be homogeneous and isothermal, meaning that thermal effects, nonlinear compressibility, and turbulence were not included in the analysis. The EOS parameters are provided in **Table 4** and were used to ensure consistent and stable fluid–structure interaction calculations throughout the simulation.

Table 2. Properties 3004Al and Aluminium Foam [25].

Parameters	Symbol	Units	Aluminium 3004	Aluminium Foam
Density	ρ	$\mathrm{kg \cdot m^{-3}}$	2700	300
Young's Modulus	E	MPa	70,000	5000
Poisson's ratio	ϑ	-	0.3	0.3
Yield Stress (Johnson-Cook)	A	MPa	125	125
Strain hardening (Johnson-Cook)	B	MPa	282.55	282.55
Strain rate sensitivity (Johnson-Cook)	C	MPa	0.0832	0.0832
Strain hardening exponent	n	-	0.44	0.44
Strain rate sensitivity exponent	m	-	2.09	2.09
Melting temperature	t_m	K	933	933

Table 3. Material Properties for STEEL 4340 and STEEL 4140 [25].

Parameters	Symbol	Units	Steel 4340	Steel 4140
Density	ρ	$\mathrm{kg \cdot m^{-3}}$	7850	7850
Young's Modulus	E	MPa	205,000	205,000
Poisson's ratio	ϑ	-	0.29	0.29
Yield Stress	σ_y	MPa	470	1000
Strain hardening coefficient	K	MPa	470	1615
Strain hardening exponent	n	-	0	0.09

Table 4. Properties of water [28].

Parameters	Symbol	Units	Value
Density	ρ	$\mathrm{kg \cdot m^{-3}}$	1000
Speed of sound	c_0	$\mathrm{m \cdot s^{-1}}$	1482
Gruneisen's gamma	γ	-	0.1

2.4. Simulation Setup

The simulation was carried out using ABAQUS SIMULIA with the Dynamic/Explicit solver, which is suitable for capturing the transient and high-strain-rate behavior caused by impulsive wave loading. The model followed the experimental setup, and the simulation was run on a PC equipped with an Intel i9-1200F 12th-generation processor with 24 CPU cores and 32 GB of RAM. The automatic time incrementation feature was enabled so that the time step was controlled by the smallest stable element and the material wave speed to maintain numerical stability. The total simulation time was set to 1 ms to accurately capture the early structural response under the impulsive load. During the simulation, key response parameters such as internal energy, stress, displacement, and potential structural failure were continuously monitored. Numerical stability was also checked by observing the energy balance and ensuring that the ratio of artificial strain energy to total internal energy stayed below 5%, which served as the stability criterion for the explicit solver.

The fluid–structure interaction was modeled using a Coupled Eulerian–Lagrangian. Contact definitions were established between the projectile–piston, piston–fluid, and fluid–specimen interfaces through surface-to-surface interactions, while a general contact algorithm was applied between the water tank–specimen and specimen–flange interfaces to prevent surface penetration. A tie constraint was also implemented between the core and face sheets to preserve interlayer cohesion during impulsive loading. This numerical configuration allowed a dynamic representation of both shock wave propagation in the fluid domain and the simultaneous structural response of the specimen.

The boundary conditions were defined following the experimental configuration. The water tank and flange were modeled as fixed components with encastre boundary conditions, restricting translational displacement along all axes. Meanwhile, the piston, flyer, and fluid were allowed to move freely in the loading direction to generate the impulsive pressure effect. Contact algorithms were applied to ensure physically consistent motion without element penetration.

An initial velocity was assigned to the flyer to initiate impact and induce a shock wave within the fluid domain, replicating the setup used in the experiment. The predefined field feature was utilized to distinguish between fluid and void regions, defining the areas filled with water and those representing air spaces. In addition, gravity loading was applied within the fluid domain to maintain hydrostatic pressure equilibrium throughout the simulation. The overall setup, including boundary conditions, loading configuration, and the fluid domain, is illustrated schematically in **Figure 4**, which shows the complete configuration of the simulation model.

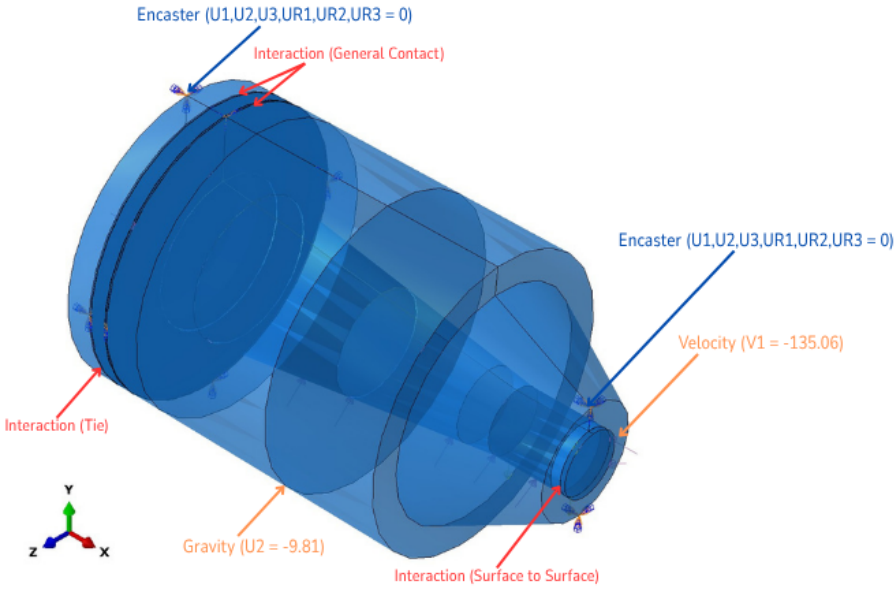

Figure 4. Simulation setup.

All components in the model, including the flyer, piston, water tank, and test specimen, were modeled using three-dimensional finite elements (C3D8R) with default artificial bulk viscosity. Meshing was applied to all components with varying element sizes to achieve a balance between result accuracy and computational efficiency. The mesh size for each component is shown in **Figure 5**, where the flyer used an element size of 4 mm, the piston 4.2 mm, the water tank 20 mm, the flange 15 mm, the aluminium sheet 2.2 mm, and the aluminium foam 2.7 mm. The water domain was first analysed through a mesh convergence study.

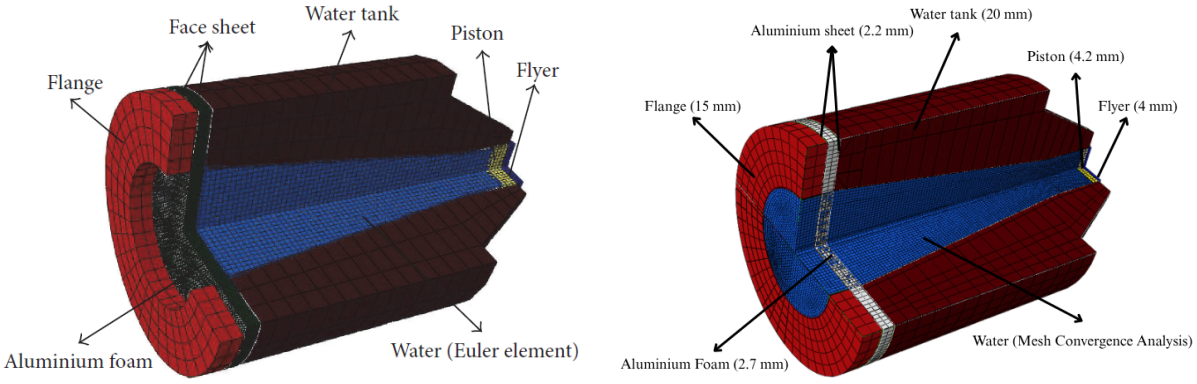

Figure 5. Meshing model: (**a**) benchmarking model [25]; (**b**) Mesh size in the present study.

The selection of element sizes was based on the deformation sensitivity and interaction characteristics between components. Components that experienced direct contact or significant deformation were modeled with finer meshes to improve the accuracy of stress prediction and dynamic response. In contrast, rigid components such as the water tank and flange were assigned coarser meshes to save computational time without reducing the overall accuracy of the simulation.

2.5. Parametric Study

This study aims to investigate the influence of variations in face sheet thickness, core thickness, and ratio thickness on the structural response of aluminium MMC sandwich composites under impulsive loading. The parameter variations were systematically designed to evaluate the sensitivity of each parameter, as summarized in **Table 5**. In the first case, the face sheet and core thicknesses were kept constant at 0.4 mm and 14 mm, respectively, to establish a reference condition and evaluate the structural response to impulsive loading. The second case investigates the effect of varying face sheet thicknesses under a constant core thickness of 16 mm and a projectile velocity of 155 m/s. The third case focuses on variations in core thickness, maintaining a face sheet thickness of 1.2 mm and a projectile velocity of 175 m/s. The fourth case examines the thickness ratio between the core and face sheet, with eight variations ranging from 1:10 to 1:1, at a constant projectile velocity of 195 m/s.

The selection of the projectile velocity range (135–195 m/s) was based on previous studies by Avachat et al. [29], which showed that increasing impact velocity leads to higher peak pressures and impulse magnitudes. This range corresponds to shock pressures between 15–20 MPa, comparable to laboratory-scale underwater explosion (UNDEX) conditions typically encountered in marine environments [30,31]. The reference thickness values for the face sheet (0.4 mm) and core (14 mm) were adopted from the experimental configuration by He et al. [25]. Further variations in face sheet (0.4–1.6 mm) and core (14–20 mm) thicknesses were selected according to design practices reported in Zhang et al. [32], Ye et al. [33], Crupi et al. [34], and Zhu et al. [24] for aluminium and aluminium foam sandwich panels used in lightweight hulls, underwater protection structures, and energy-absorbing components in marine systems.

Table 5. Case Scenario Configuration.

Case Group	Variable	Parameter Variation	Fixed Parameters
C1 – Velocity variation	Projectile Velocity (m/s)	135, 155, 175, 195	Face sheet = 0.4 mm Core = 14 mm
C2 – Face Sheet Thickness Variation	Face sheet (mm)	0.4, 0.8, 1.2, 1.6	Velocity = 155 m/s Core = 16 mm
C3 – Core Thickness Variation	Core (mm)	14, 16, 18, 20	Velocity = 175 m/s Face sheet = 1.2 mm
C4 – Ratio of Face/Core Thickness	Thickness ratio variation	(1.6/16), (1.6/11.2), (1.6/6.4), (1.6/1.6), (16/16), (16/1.6), (11.2/1.6), (6.4/1.6)	Velocity = 195 m/s

The variations in the core-to-face sheet thickness ratio were included to study their effect on impact resistance and structural stiffness. Besides the usual ratios where the core is thicker than the face sheets, reversed ratios where the face sheets are thicker than the core were also tested to gain a wider understanding of the structural response. Through these variations, this study aims to find the best configuration of the MMC sandwich composite that can resist impulsive loads effectively and explain how thickness parameters influence its mechanical performance.

3. Result and Discussion

3.1. Mesh Convergence Analysis

A mesh convergence analysis was carried out to ensure that the numerical results of the Underwater Shock Loading Simulator (USLS) model achieved an optimal level of accuracy and computational efficiency. Selecting an appropriate mesh size is crucial to minimizing computation time without sacrificing result accuracy. In this study, the relationship between the number of mesh elements and the peak pressure values measured at Sensor B in the fluid domain was evaluated. Increasing the number of mesh elements improves result accuracy but also significantly increases the computation time. Therefore, it is necessary to identify a mesh size close to the convergence condition to achieve a balance between accuracy and efficiency.

As shown in **Figure 6**, the data from the mesh convergence simulations for mesh sizes between 12 mm and 2 mm were taken from the average peak pressure in the fluid domain measured at Sensor B. The illustration of the selected element for peak pressure measurement is presented in **Figure 7**. To assess the convergence level, the Richardson Extrapolation method and Grid Convergence Index (GCI) were applied. The Richardson Extrapolation method is used to estimate the exact solution based on the mesh refinement trend, while the GCI is used to quantify the numerical error between the finest meshes. Three finest mesh sizes were analyzed—4.5 mm, 3 mm, and 2 mm—with a constant refinement ratio (r = 1.5). The simulation results show that for the 4.5 mm mesh with 87,210 elements, the measured peak pressure was 51.52 MPa. When the mesh was refined to 3 mm (277,760 elements), the pressure increased to 53.48 MPa, and for the 2 mm mesh (1,087,240 elements), the peak pressure reached 52.55 MPa.

The results of the Richardson and GCI calculations are summarized in **Table 6**. The Richardson value of 51.69 MPa provides an estimated theoretical peak pressure for an extremely fine mesh and shows a consistent convergence trend toward the experimental reference. The GCI for the two meshes (2 mm and 3 mm) is approximately 2%, indicating good consistency between them. Based on this convergence behavior, and considering the balance between accuracy and computational efficiency, the 3 mm mesh was selected as the primary mesh size for the subsequent analyses.

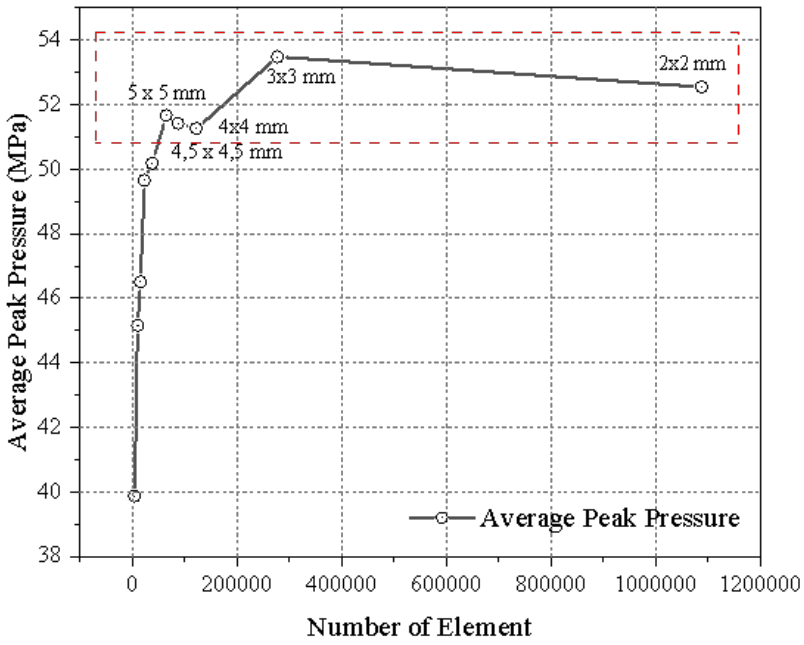

Figure 6. Mesh convergence analysis results.

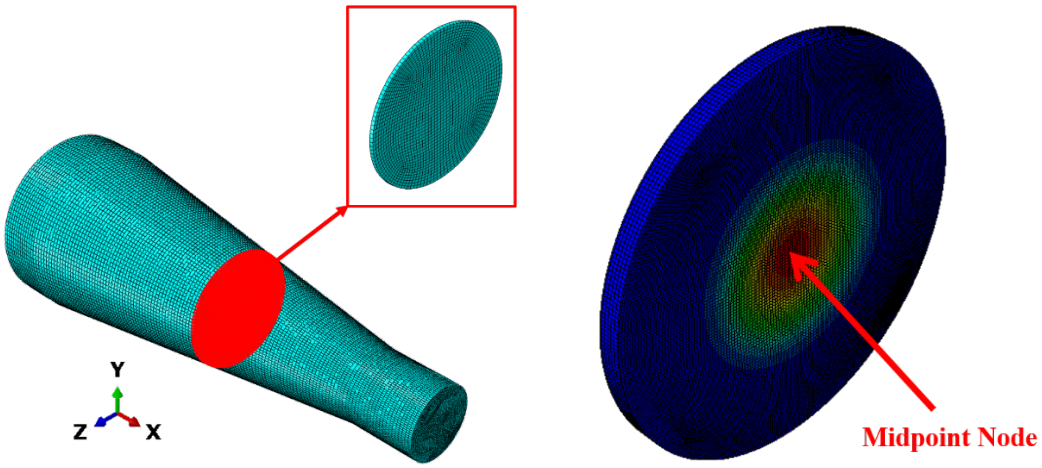

(**a**) (**b**)

Figure 7. Measurement points in the simulation: (**a**) Sensor B for pressure measurement; (**b**) Midpoint of the specimen for displacement measurement.

Table 6. Simulation time comparison.

Mesh Size	Element	Peak Pressure	Relative Difference	GCI	Richardson Exploration	Simulation Time
4.5 mm	87,210	51.54 MPa	-	-	-	62 Minute
3 mm	277,760	53.48 MPa	1.73%	4.17%	51.69 MPa	118 Minute
2 mm	1,087,240	52.55 MPa	3.76%	2%	-	556 Minute

3.2. Simulation Validation

Validation was carried out by comparing the numerical simulation results with the experimental data reported by He et al.[25]. In the experiment, pressure measurements were obtained using two sensors (B and C) placed along the fluid domain to record the peak pressure during shock wave propagation. The experimen-

tal results showed that the highest pressure occurred at Sensor B with a value of 61.4 MPa, while Sensor C recorded a lower value due to wave attenuation along the propagation distance.

In this study, the validation process focused on Sensor B, as it represents the area with the most significant shock wave response. The total simulation time was set to 1 ms, representing the duration required for the full propagation and dissipation of the shock wave within the fluid domain. Preliminary tests confirmed that the pressure and internal energy responses reached stable conditions before this time, ensuring that no significant wave reflections affected the results. The observed output parameters included the peak pressure at Sensor B and the maximum displacement at the midpoint of the face sheet, as these parameters correspond to the most responsive regions under impulsive loading and directly match the quantities measured in the research by He et al.

The validation results are presented in **Figure 8**. The simulation predicted a peak pressure of 63.9 MPa and a maximum displacement of 4.52 mm at the face sheet midpoint at 0.74 ms. In comparison, He et al. reported an experimental peak pressure of 65.1 MPa and a maximum displacement of 4.14 mm at the same time. In their simulation, He et al. recorded a peak pressure of 61.4 MPa, but the maximum displacement at 0.74 ms was not reported; therefore, the displacement comparison is based solely on experimental results. A detailed comparison of the validation outcomes is summarized in **Table 7**. The differences, all below 10%, indicate that the numerical model is well-validated and can reliably capture the physical behavior of the system. Following model validation, a mesh convergence analysis was performed to identify the optimal element size, balancing accuracy and computational efficiency.

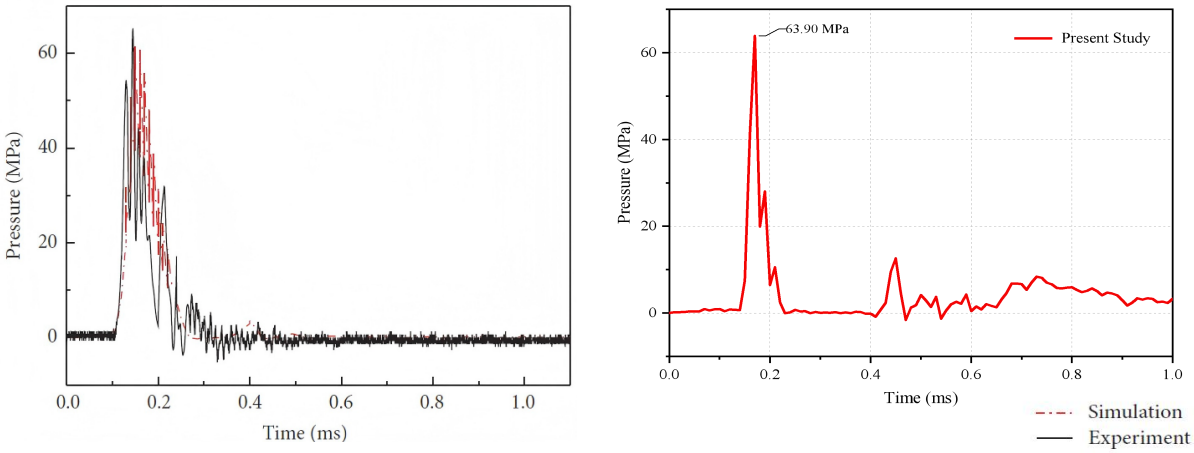

(**a**) (**b**)

Figure 8. The pressure-time histories in Sensor B: (**a**) He et al. Study; (**b**) Present Study.

Table 7. Comparison of simulation results with previous research.

Parameter	Present Study	He et al. Experiment	Error	He et al. Simulation	Error
Peak Pressure (Sensor B)	63.90 MPa	65.1 MPa	1.84%	61.4 MPa	4%
Displacement (0.74 ms)	4.52 mm	4.14 mm	8.40%	-	-

3.3. Wave Generation

The magnitude of the impulse generated by USLS is known from the amount of pressure measured in the water tank. The blast wave originates from the flyer impact on the piston, which generates pressure transmitted through the fluid domain to the specimen. Theoretically, the peak pressure measured at each sensor can be calculated with Equation (1), and the amount of impulse can be defined as nondimensional impulse with Equation (2) here:

$$P_m = -\left(\frac{D_0}{D}\right)^2 \frac{(\rho_0 C_0)_1 (\rho_0 C_0)_2}{(\rho_0 C_0)_1 + (\rho_0 C_0)_2} v_1 \qquad (1)$$

$$\widehat{I} = \frac{I_0}{\overline{M} \cdot \sqrt{\sigma_y / \rho}} \quad (2)$$

Where D_0 is the diameter of the inlet section of the conical-shaped water tank, and D is the diameter of the water tank at the point where the sensor is located. The negative sign in Equation (1) indicates that the stress wave is a compression wave. $(\rho_0 C_0)_2$ represents the wave impedance with a value of 40.82×10^6 $kg/_{s \cdot m^2}$ and $(\rho_0 C_0)_1$ refers to water with a value of 1.46×10^6 $kg/_{s \cdot m^2}$. Meanwhile, v_1 is the initial velocity of the flyer. From the simulation, the pressure–time history at Sensor B is shown in **Figure 9**.

The measurement results indicate that as the initial velocity of the flyer increases, the peak pressure generated also rises, with values of 63.9 MPa at 135 m/s, 72.06 MPa at 155 m/s, 80.1 MPa at 175 m/s, and 88.1 MPa at 195 m/s. This trend confirms that higher flyer velocities correspond to greater impact intensities, which is consistent with theoretical expectations. However, when comparing the simulation results to theoretical calculations, a measurable difference is observed discrepancy is observed, as illustrated in **Figure 10**, with pressure propagation in the water tank shown in **Figure 11** The discrepancy increases with flyer velocity, reaching up to 17.32% at 195 m/s (see **Table 8**).

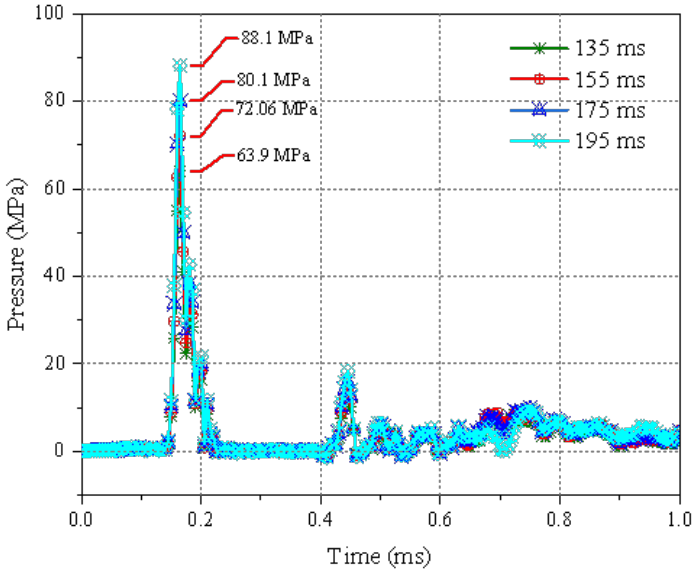

Figure 9. Peak Pressure in Sensor B.

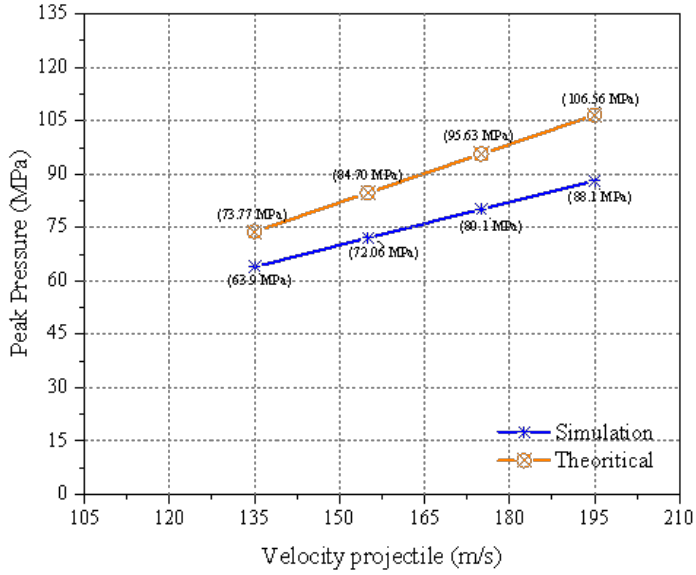

Figure 10. Comparison of simulated peak pressure with theoretical.

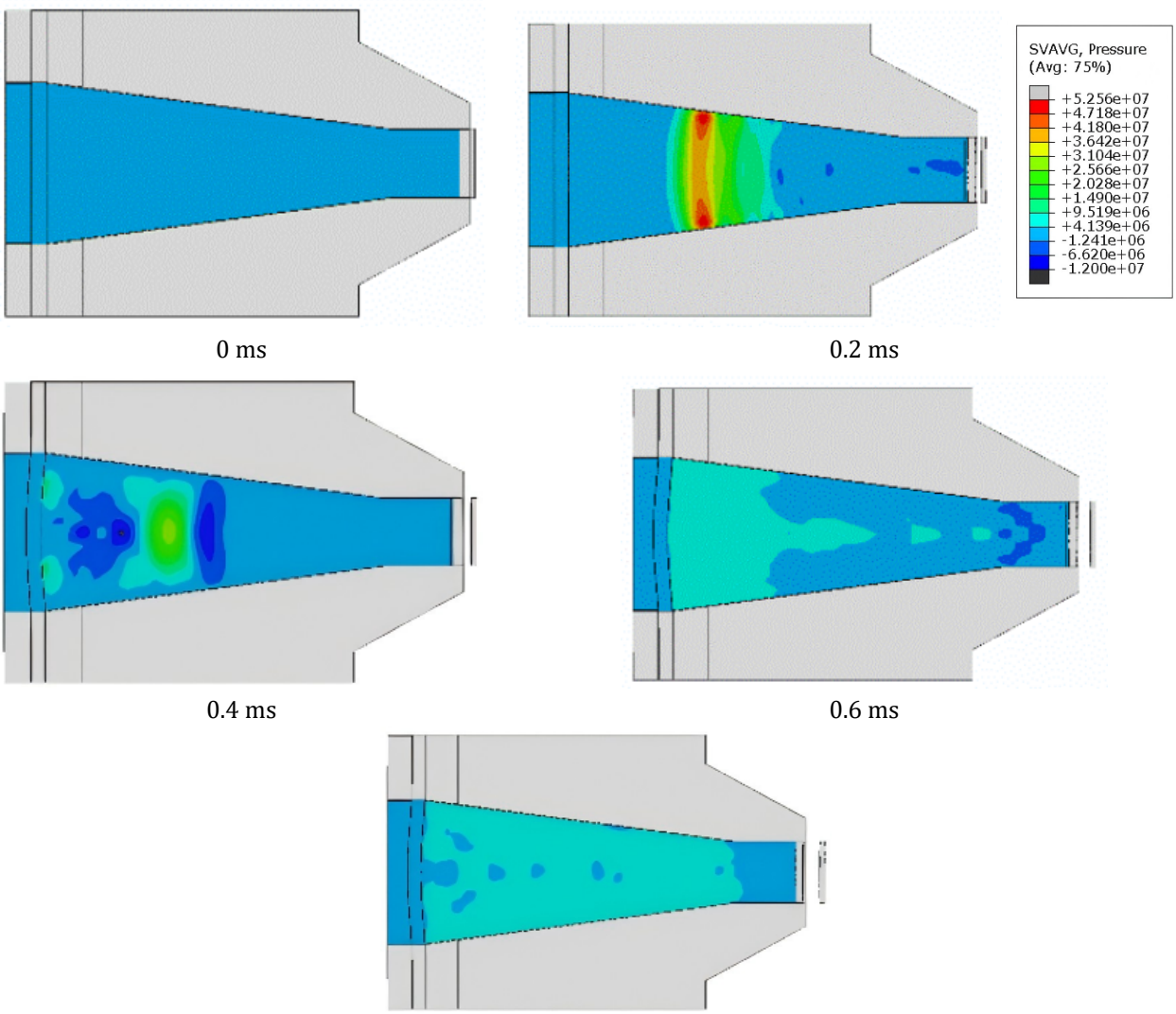

Figure 11. Pressure transfer in a water tank.

Table 8. Comparison of Peak Pressure Errors Relative to Theoretical Values.

Velocity Flyer (m/s)	Theoretical Value (MPa)	Simulation (MPa)	Error (%)
135	73.77	63.9	14.80%
155	84.70	72.06	14.92%
175	95.63	80.1	16.24%
195	106.56	88.1	17.32%

From these results, the deviation relative to theoretical values was noticeable, prompting an ablation analysis to identify contributing factors. This analysis included the evaluation of several key variables, such as the water properties (EOS) with parameters c_0, γ, and cavitation, as well as tank flexibility, numerical damping, and the material properties of the flyer and piston.

The ablation simulation was performed using a 3 mm mesh for the fluid domain to identify the most influential parameters through a sensitivity analysis. The flyer velocity used was 195 m/s, which previously produced the highest error compared to theory. Ablation analysis was carried out by increasing or decreasing the parameter values by ±10% from their initial values and by activating or deactivating specific parameters. Details of the ablation cases are presented in **Table 9**, while the

results are shown as peak pressure values for each case variation, which were then compared based on the error relative to the initial simulation. Visualization of the simulation results is presented in **Figure 12**.

Table 9. Overview of ablation cases, parameter settings, and simulation results.

Main Case	Parameter	Variation Range	Case ID	Initial Value	Varied Value	Peak Pressure	Change
Baseline	—	—	Baseline	—	—	88.1 MPa	—
EOS	Speed of sound, c_0	−10%	ECL	1480 ms	1332 ms	80.89 MPa	8.18%
	Speed of sound, c_0	+10%	ECH	1480 ms	1628 ms	97.13 MPa	10.25%
	Gamma (γ)	−10%	EGL	0.1	0.09	88.05 MPa	0.06%
	Gamma (γ)	+10%	EGL	0.1	0.11	88.07 MPa	0.03%
	Cavitation	No/Yes	EC	—	Yes/No	88.05 MPa	0.06%
Tank	Boundary condition	Rigid/Flexible	TB	—	Flexible/Rigid	86.8 MPa	1.47%
Numerical damping	Artificial bulk viscosity	b_1,b_2 variation	DAH	$b_1 = 1, b_2 = 1$	$b_1 = 0.5, b_2 = 1$	91.45 MPa	3.81%
	Artificial bulk viscosity		DAL	$b_1 = 1, b_2 = 1$	$b_1 = 1, b_2 = 0.5$	88.29 MPa	0.22%
	Hourglass control	Default/Combined	DHC	Default	Combined	88.05 MPa	0.06%
Steel	Young's modulus (E)	−10%	SEL	205,000 MPa	184,500 MPa	88.15MPa	0.06%
	Young's modulus (E)	+10%	SEH	205,000 MPa	2.25500 MPa	88.06 MPa	0.04%
	Yield stress	−10%	SYL	1000 MPa	900 MPa	87.36 MPa	0.83%
	Yield stress	+10%	SYH	1000 MPa	1100 MPa	88.15 MPa	0.06%
	Density	−10%	SDL	7850 kg/m^3	7065 kg/m^3	87.3 MPa	0.91%
	Density	+10%	SDH	7850 kg/m^3	8635 kg/m^3	88.79 MPa	0.78%

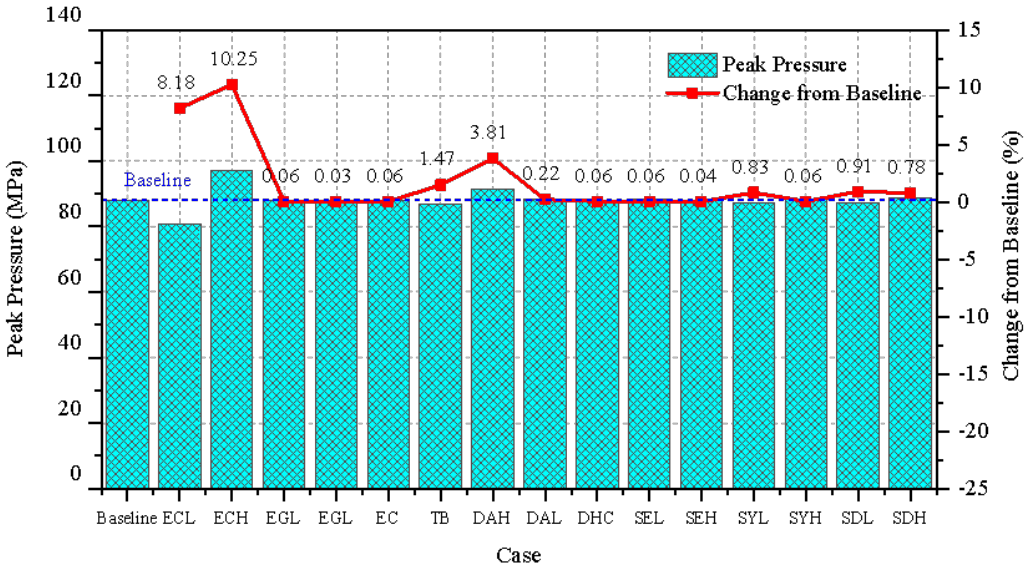

Figure 12. Ablation analysis result.

The simulation results show that the EOS properties or fluid domain parameters are the most influential factors affecting wave propagation and peak pressure in the water tank, and increasing the water speed by 10% results in a peak pressure increase of more than 10%, from 88.1 MPa to 97.13 MPa. Conversely, the least influential parameter is Gamma in the EOS.

Based on the latest simulation results with the mesh size optimized in the previous study, a peak pressure of 88.1 MPa was obtained at a velocity of 195 m/s, which served as the baseline for the ablation analysis. Compared to the theoretical value, this result has an error of 17.32%. Adjusting the speed of sound in the water properties can increase the peak pressure, but it also directly changes the theoretical value. Therefore, the adjustment was applied through numerical damping, which increased the peak pressure to 91.45 MPa without changing the theoretical value, representing a 3.81% change from the baseline and an error of 14.34%. This adjustment was then applied to the entire mesh. At a velocity of 135 m/s with a 3 mm mesh, the peak pressure reached 64.73 MPa, which is very close to the experimen-

tal result of 65.1 MPa.

From a theoretical perspective, He et al.'s previous study also reported an 11.7% error between theory and experiment, indicating that the theory needs to be optimized by considering energy losses and other factors affecting wave propagation. In the present study, experimental results were used as the basis for validating the simulation, while the theoretical values were used only for comparison to assess the tendency of the numerical results toward the ideal case. Therefore, this analysis confirms that the developed numerical model is well-validated using experimental data. Furthermore, the incorporation of ablation-analysis adjustments in the present work has been shown to improve the simulation accuracy, enabling the numerical results to more closely approach both the theoretical predictions and the experimental measurements.

3.4. Case 1

The first case study aimed to evaluate the ultimate capacity of Metal Matrix Composite (MMC) against impulse variations caused by differences in the initial velocity of the flyer. The difference in impulse values due to projectile velocity variation resulted in significant maximum displacement of the MMC material, namely 5.830 mm at 135 m/s, 6.7858 mm at 155 m/s, 7.4943mm at 175 m/s, and 10.749 mm at 195 m/s (see **Figure 13**). The maximum displacement is measured from the highest deflection of the material, which is affected by two main pressures.

The first pressure occurs when the initial wave hits the material, while the second pressure is the residual pressure due to wave resonance. Although the second pressure is smaller, its combined effect with the first pressure produces a larger total force, so the material deforms more significantly, as seen from the larger displacement. The maximum difference in displacement with each increase in projectile speed is also quite significant, namely 0.95 mm between 135 m/s and 155 m/s, 0.71 mm between 155 m/s and 175 m/s, and 3.25 mm between 175 m/s and 195 m/s. This shows that the greater the impulse or projectile speed, the difference in material displacement also increases significantly. The displacement contour of the variation test results can be seen in **Figure 14**.

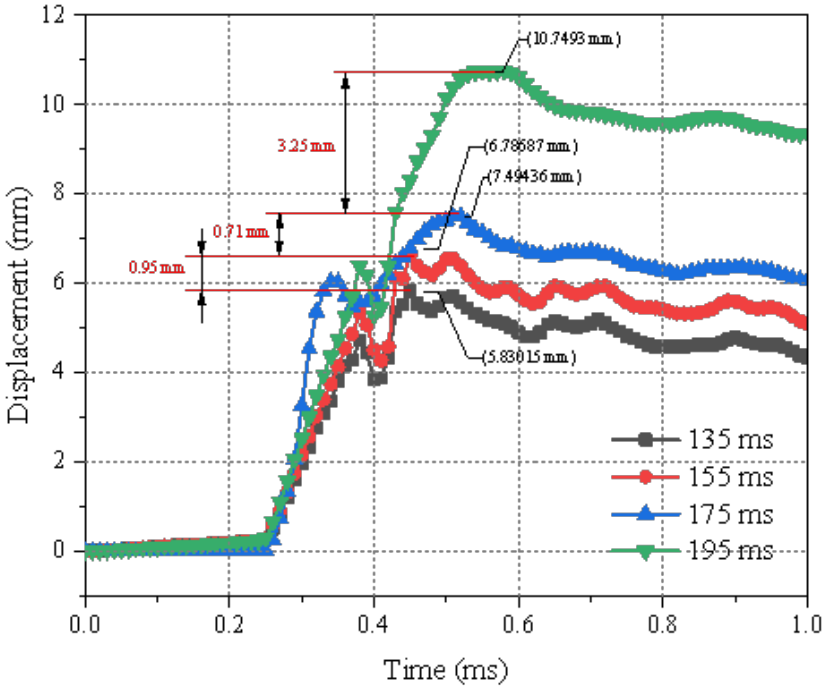

Figure 13. Time History of Displacement for Varying Impulse.

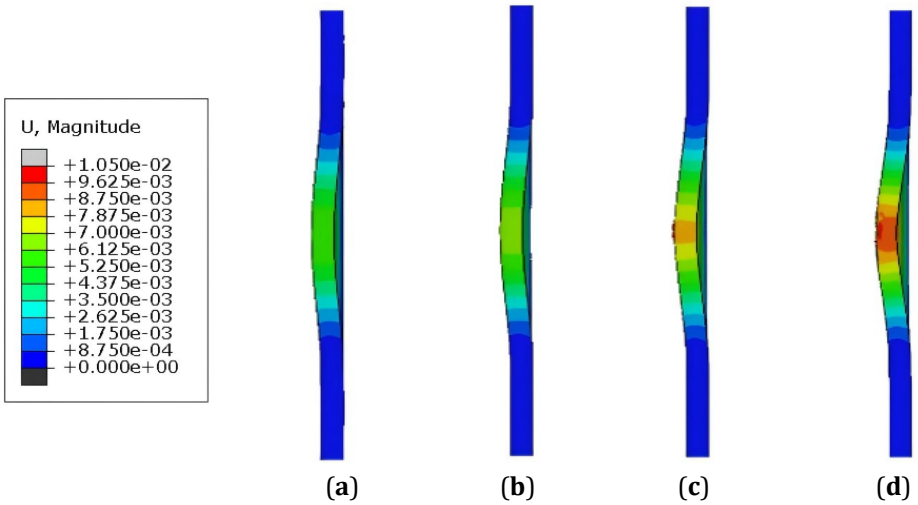

Figure 14. Cross-sectional view showing maximum displacement in impulse magnitude variation: (**a**) 0.0125; (**b**) 0.0144; (**c**) 0.0163; (**d**) 0.0181.

3.5. Case 2

The second case evaluates the effect of face sheet thickness on the ultimate capacity of aluminium MMC when subjected to impulse loads. The simulation results demonstrate a clear relationship between face sheet thickness and material deformation, where thicker face sheets result in smaller maximum deformation. Specifically, the maximum deformation recorded was 5.16 mm for a thickness of 0.4 mm, 4.69 mm for 0.8 mm, 4.15 mm for 1.2 mm, and 3.51 mm for 1.8 mm (see **Figures 15** and **16**). These findings indicate that increasing the face sheet thickness enhances the structure's resistance to impulsive loads by distributing stress more effectively across the material. However, the increase in resistance is not linear.

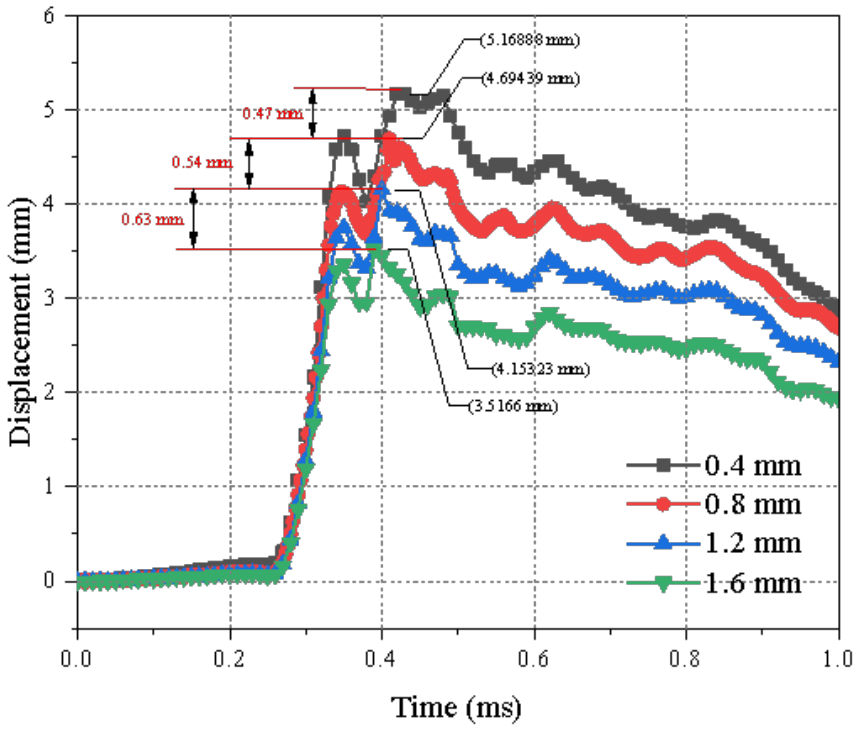

Figure 15. Time History of Displacement for Varying Face Sheet Thickness.

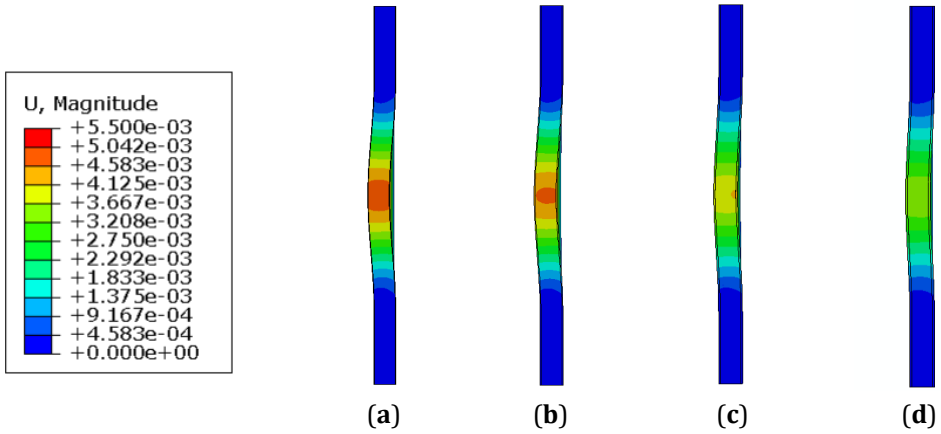

Figure 16. Cross-sectional view showing maximum displacement in face sheet thickness variation: (**a**) 0.4 mm; (**b**) 0.8 mm; (**c**) 1.2 mm; (**d**) 1.6 mm.

As an example, increasing the thickness from 0.4 mm to 0.8 mm reduces the deformation by 0.47 mm, while a further increase to 1.2 mm results in a reduction of 0.54 mm, and increasing it to 1.8 mm leads to a reduction of 0.63 mm. This trend indicates that a thicker face sheet provides higher bending stiffness, allowing it to better resist the initial deformation caused by the impulsive load.

To strengthen this observation, a time-resolved energy ledger analysis was added by presenting the evolution of total energy, which is the sum of kinetic and internal energy in the face sheet region. As shown in **Figure 17**, all thickness variations exhibit a sharp rise in energy at around 0.25–0.30 ms, which corresponds to the arrival of the initial impulse, followed by a stable phase after 0.35 ms. Thicker face sheets reach higher steady-state total energy values, namely 48 Joule for 0.4 mm, 73 Joule for 0.8 mm, 87 Joule for 1.2 mm, and 91 Joule for 1.6 mm. In addition, the graph shows that post-impulse energy fluctuations are smaller for models with greater thickness, indicating improved dynamic damping capacity that contributes to structural stability.

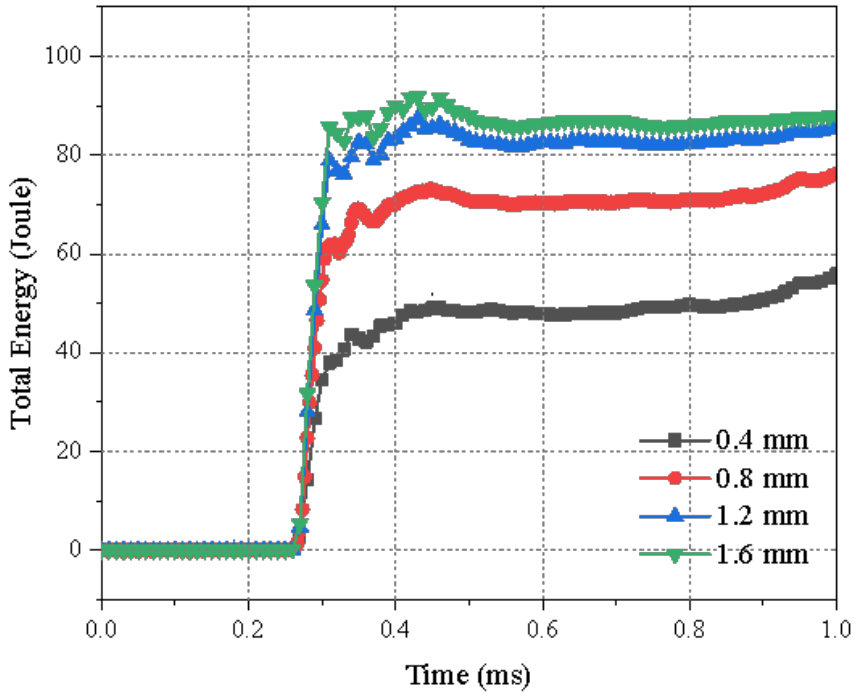

Figure 17. Time-Resolved Energy Ledger for Different Face Sheet Thicknesses.

The consistency of this trend is further supported by the quantification of attenuation in the secondary pressure peak generated by fluid resonance. **Figure 18** shows that within the time range of 0.35 to 0.50 ms, the amplitude of the second-peak pressure decreases significantly as the thickness increases. This reduction reaches 8% when the thickness increases from 0.4 to 0.8 mm, 19.09% from 0.8 to 1.2 mm, and 16.71% from 1.2 to 1.6 mm. This mechanism can be explained by the increase in mechanical impedance in thicker face sheets, which allows part of the reflected wave energy to be absorbed instead of returning to the fluid as a high-amplitude resonance. This effect limits the amplification of the reflected wave and results in a lower secondary pressure peak.

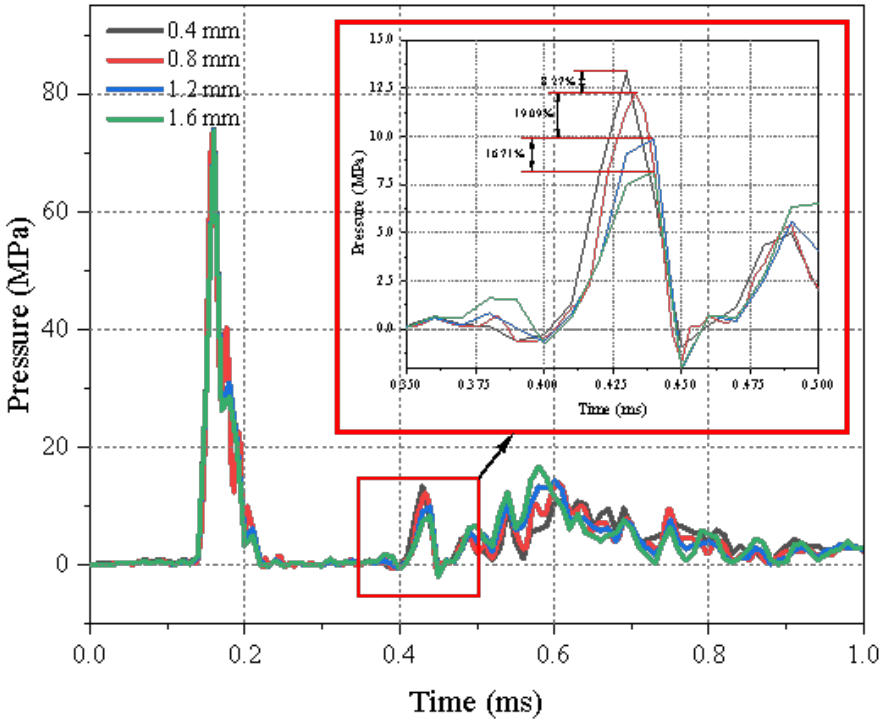

Figure 18. Attenuation of Secondary Pressure Peaks for Different Face Sheet Thicknesses.

The combined effects of reduced maximum displacement, increased internal energy, and decreased secondary pressure amplitude provide a consistent understanding of the role of face sheet thickness in modifying impulsive and resonant responses. This analysis offers a strong physical basis for how increasing thickness helps control midpoint deformation in the panel under dynamic impulsive loading.

3.6. Case 3

The third case evaluates the effect of aluminium MMC core thickness on the material's response to impulsive loads, with the face sheet thickness kept constant at 1.2 mm and the projectile velocity set at 175 m/s. The simulation results show that as the core becomes thicker, the maximum deflection of the material decreases. The recorded deflections are 5.425 mm for a 14 mm core, 4.573 mm for a 16 mm core, 4.163 mm for an 18 mm core, and 3.689 mm for a 20 mm core (see **Figures 19** and **20**). Increasing the core thickness clearly reduces the maximum deflection, but the reduction becomes smaller as the core thickness increases. This indicates that while core thickness is an important factor, increasing it alone does not significantly enhance the strength of aluminium MMC with foam cores beyond a certain point.

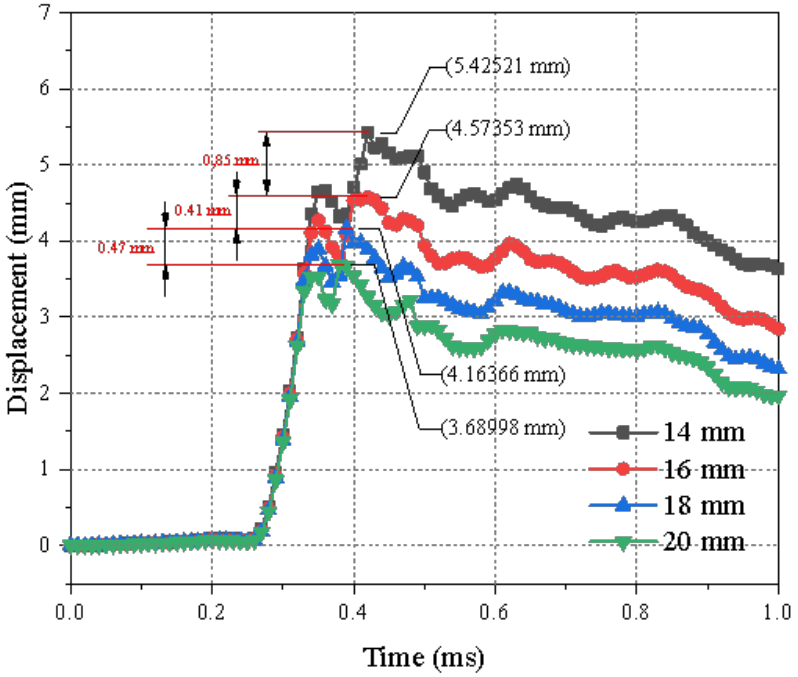

Figure 19. Time History of Displacement for Varying Core Thickness.

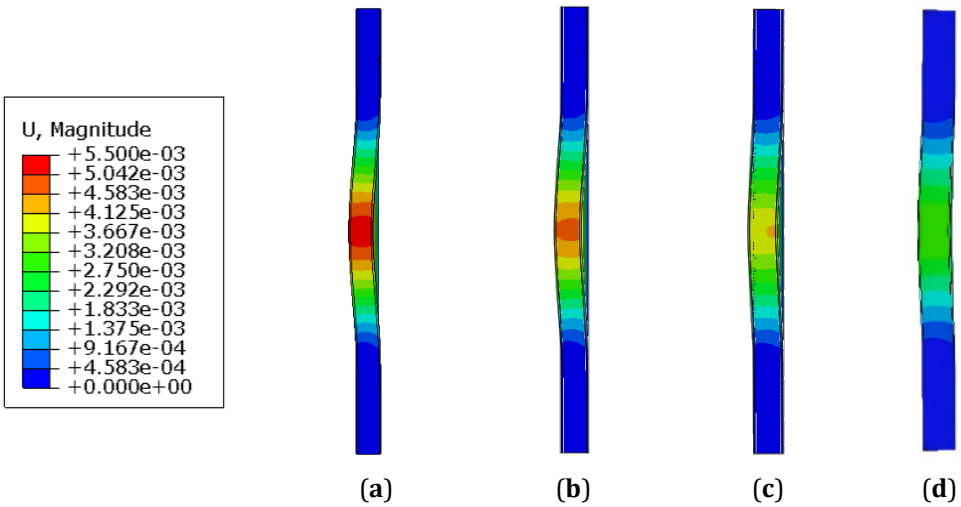

Figure 20. Cross-sectional view showing maximum displacement in core thickness variation: (**a**) 14 mm; (**b**) 16 mm; (**c**) 18 mm; (**d**) 20 mm.

Moreover, the simulation results reveal that using a 1.2 mm thick face sheet results in a relatively small gap between the peak deflections caused by the first and second pressure waves. As the core thickness increases, the gap between the peaks of the first and second shock waves tends to decrease. This suggests that thicker core structures not only improve deformation resistance but also dampen wave resonance more effectively. However, the benefits of increased core thickness become progressively limited in their overall contribution to the structure's performance. Therefore, this analysis highlights the importance of determining the optimal core thickness to achieve a balance between structural strength, energy absorption capability, and material efficiency.

To clarify the structural response and evaluate the safety margin of the panel, the core compression (stress–strain) curve was incorporated into the analysis. The densification onset was determined using the linear-

regression intersection method, which is a quantitative approach commonly applied to cellular materials such as metallic foams, polymeric foams, and honeycombs. In this method, a strain range that lies entirely within the densification region (ε = 0.60–0.80) is selected, as the stress–strain curve in this interval shows a sharp and nearly linear increase. A linear regression is then performed to obtain the slope and intercept that represent the cell-collapse behavior of the foam structure. The densification onset is defined as the strain at which the experimental curve first intersects the fitted densification line, or the point with the minimum stress difference. This approach provides an objective, measurable, and consistent determination of the onset. The densification region and the core compression stress–strain curve can be clearly seen in **Figure 21**.

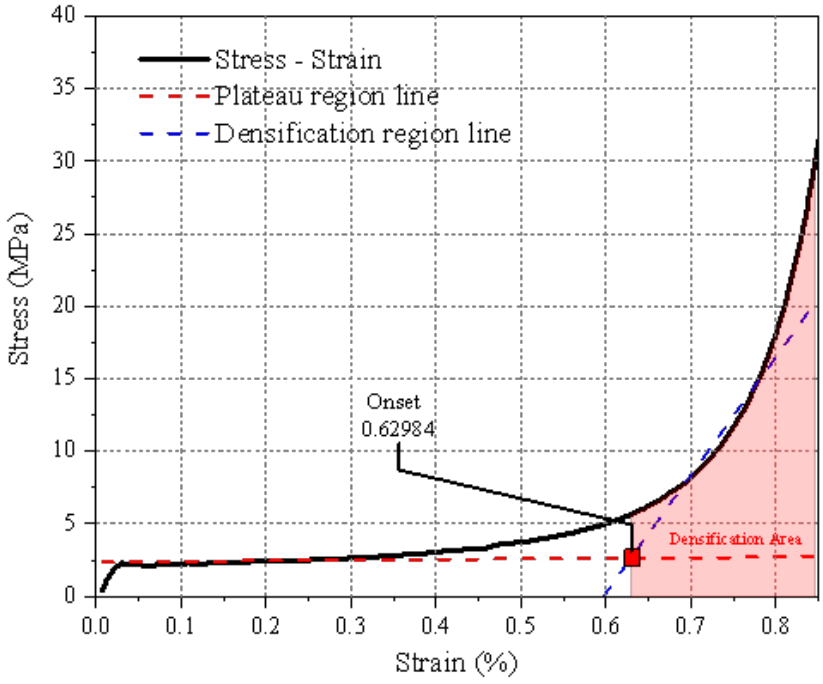

Figure 21. Stress–strain response of the core with identified densification area.

The densification onset obtained from the stress–strain analysis was then overlaid onto the maximum displacement-at-midpoint versus core-thickness plot to identify the onset of marginal benefit decay, which represents the point at which increasing the core thickness no longer provides a significant reduction in deflection. Simulation results show that for core thicknesses of 14 mm, 16 mm, 18 mm, and 20 mm, the corresponding maximum midpoint displacements are 5.42 mm, 4.57 mm, 4.16 mm, and 3.68 mm, respectively. The overlay indicates that all displacement values remain well below the densification onset line, confirming that the panel still operates within the plateau region and has not entered the densification zone that could lead to early failure (see **Figure 22**). This verifies that the loading condition in this study does not push the structure toward the critical densification limit.

Furthermore, the overlay plot clearly shows that thicker cores exhibit higher densification onset values, meaning they can sustain larger strains before cell collapse begins. Physically, this occurs because thicker cores contain a greater cell volume, allowing them to absorb deformation energy for a longer duration before reaching densification. However, the additional benefit of increasing core thickness becomes progressively smaller, which aligns with the pattern observed in the impulsive-load simulations. The reduction in displacement from 14 to 16 mm is significant, whereas the reduction from 18 to 20 mm is much smaller, indicating that further increasing core thickness at this stage no longer provides substantial improvement in densification resistance.

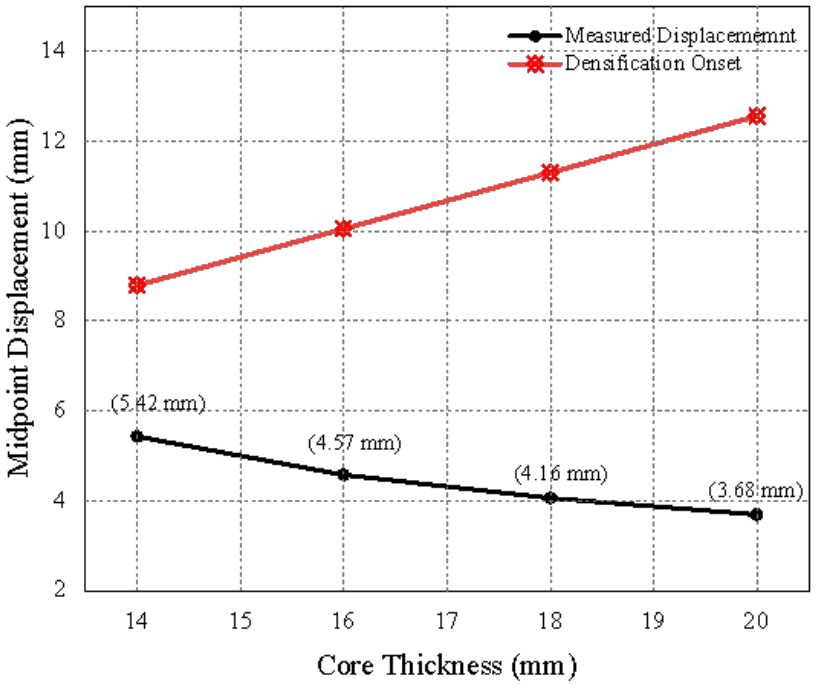

Figure 22. Maximum Midpoint Displacement Compared with Densification Onset Line.

3.7. Case 4

The fourth case evaluates the impact of thickness ratios and identifies sandwich composite configurations with comparable performance in resisting impulsive loads despite differing thickness distributions. Simulations show maximum displacements of 4.13 mm (1:10), 6.63 mm (1:7), 10.34 mm (1:4), and 17.22 mm (1:1) (see **Figure 23**). These results highlight that smaller thickness ratios significantly reduce deformation resistance, primarily due to the reduced core thickness. Displacement contours of the test specimen are detailed in **Figure 24**.

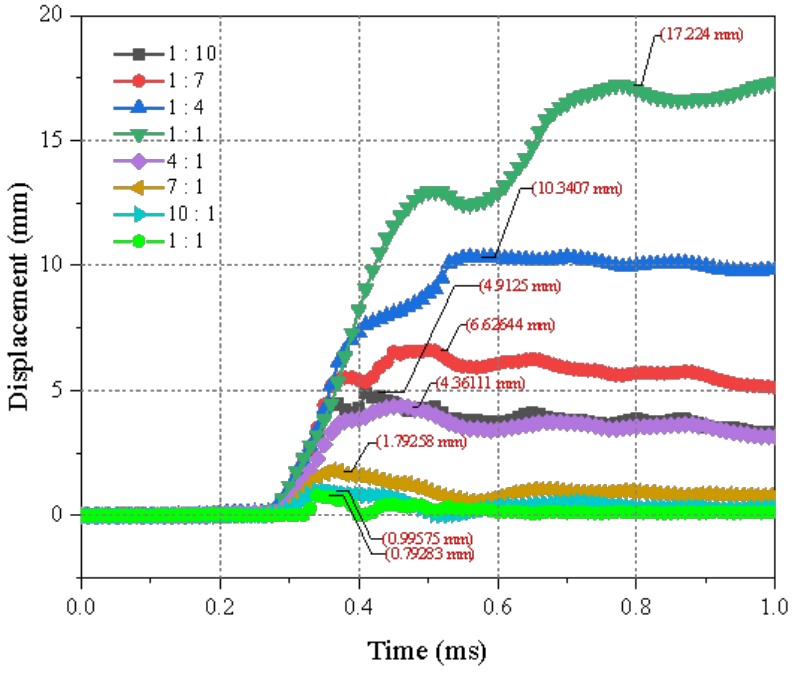

Figure 23. Time History of Displacement for Varying Thickness Ratio.

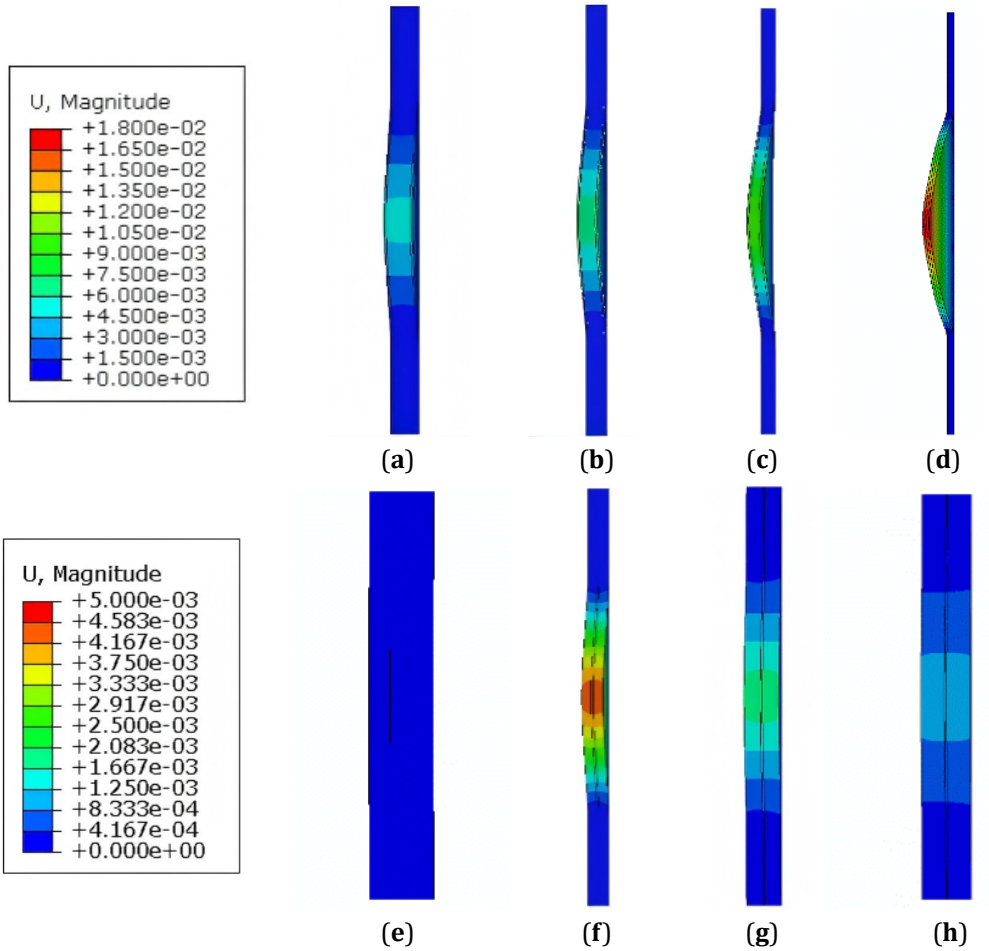

Figure 24. Cross-sectional view showing maximum displacement in thickness ratios' variation: (**a**) 1:10; (**b**) 1:7; (**c**) 1:4; (**d**) 1:1; (**e**) 1:1; (**f**) 4:1; (**g**) 7:1; (**h**) 10:1.

Reversing the thickness ratio by increasing the face sheet thickness to match the original 16 mm core shows improved performance. Maximum displacements are 0.79 mm for 1:1, 0.99 mm for 10:1, 1.79 mm for 7:1, and 4.36 mm for 4:1. These findings confirm that increasing core thickness greatly enhances deformation resistance, with smaller deflections observed for thicker face sheets. However, higher face sheet thickness increases structural weight, reducing efficiency for lightweight applications. Interestingly, the 1:10 and 4:1 configurations perform almost equivalently under impulsive loads, with only a 0.6 mm difference in maximum deflection. This suggests both configurations provide similar performance in resisting impulsive loading.

A further analysis was conducted by normalizing the maximum displacement with respect to the areal mass to obtain a specific stiffness metric. The graph of normalized displacement versus specific stiffness shows a clear trend: the smaller the normalized displacement, the higher the specific stiffness, indicating that the panels become stiffer per unit mass (see **Figure 25**). This analysis allows for a quantitative comparison of stiffness across different configurations.

In addition, the Pareto graph of areal mass versus normalized displacement shows the trade-off between mass and deformation: an increase in mass generally reduces the normalized displacement, making the panels stiffer. Interestingly, the 1:10 and 4:1 configurations exhibit similar maximum deflection (a difference of ~0.6 mm), but 4:1 has a much higher areal mass compared to 1:10 or 1:7. The graph of normalized displacement versus areal mass confirms this trade-off trend: as mass increases, normalized displacement tends to decrease, showing that the panels become stiffer per unit mass (see **Figure 26**). From this graph, it is clear that although 4:1 has slightly smaller deflection, the 1:10 configuration is still more efficient because it provides relatively high stiffness with much lower mass.

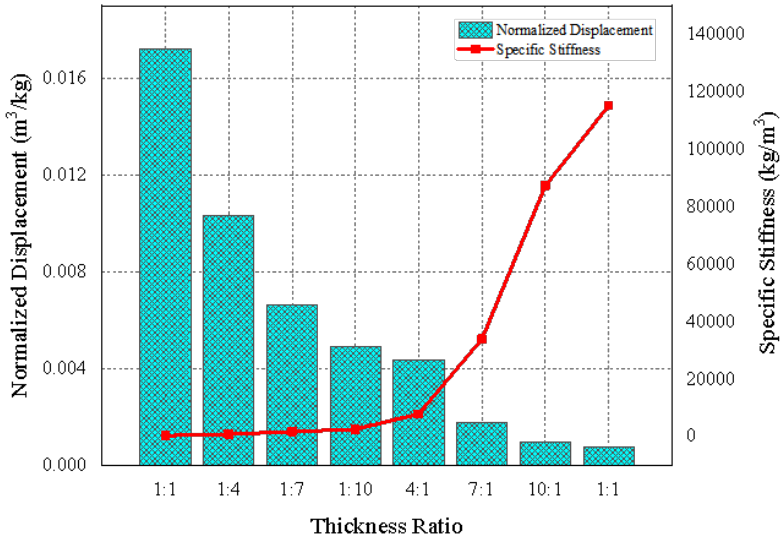

Figure 25. Effect of Thickness Ratio on Normalized Displacement and Specific Stiffness.

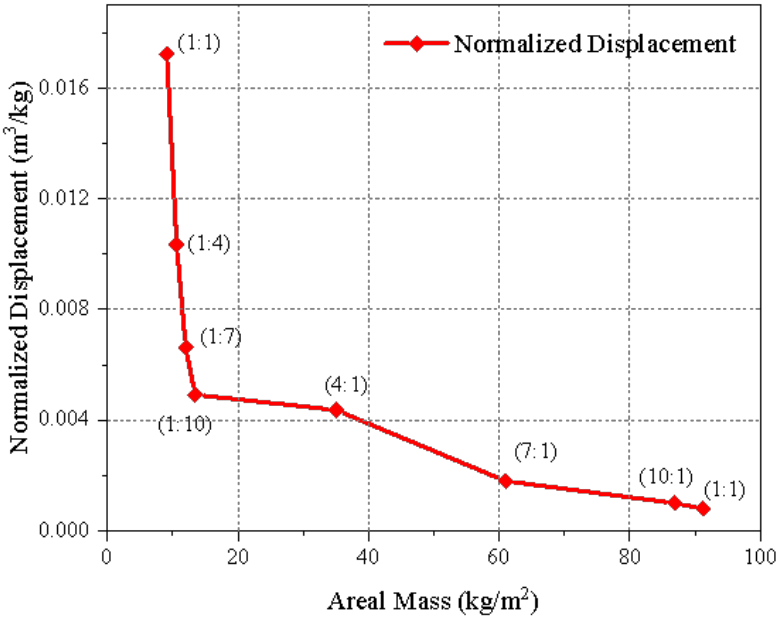

Figure 26. Pareto Plot of Areal Mass versus Normalized Displacement for Sandwich Panels.

Thus, this comparison demonstrates how the choice of thickness ratio affects the combination of maximum stiffness and structural weight, and confirms that the 1:10 thickness ratio remains more efficient than 4:1 for lightweight sandwich composite designs that must withstand impulsive loads.

4. Conclusion

Based on the results of this study, the following conclusions can be drawn:

- Projectile velocity significantly affects the impulse in the USLS tool, which directly influences specimen deflection.
- Increasing the face sheet thickness from 0.4 mm to 1.8 mm reduced the maximum deflection from 5.16 mm to 3.51 mm, although the improvement in strength was not strictly linear.
- Thicker face sheets are more effective in reducing displacement caused by resonant waves.
- Increasing the core thickness from 14 mm to 20 mm decreased deflection from 5.42 mm to 3.68 mm, but

the effect diminishes with further increases in thickness.

- An optimal combination of core and face sheet thickness is recommended to enhance the performance of MMC materials.
- Materials with a thickness ratio of 4:1 showed performance comparable to MMCs with a 1:10 ratio, with deflections of approximately 4.36 mm and 4.91 mm, respectively. However, the 1:10 configuration is more efficient because it provides higher stiffness with lower mass, making it the optimal choice for lightweight sandwich composite designs.

In brief, these findings highlight the significant influence of thickness on MMC performance. The simulation results in mesh convergence and validation analysis show good agreement with the experimental results from the previous study. However, compared with the theoretical prediction, the difference is around 14%. A more detailed sensitivity analysis will be conducted in future research to identify the most influential parameters and refine the governing equations (Equations (1) and (2)). This further analysis will help adjust the equations and simulation assumptions to better match ideal and realistic conditions, and improve predictive accuracy.

Author Contributions

Conceptualization, R., R.A. and A.F.M.; methodology, R., R.A.; software, R., A.D.N., A.R.P. and R.A.; validation, R.A., A.D.N., A.R.P. and A.F.M.; formal analysis, R., R.A. and A.F.M.; investigation, R., R.A. and A.F.M.; resources, R., R.A. and A.R.P.; data curation, R., R.A. and A.R.P.; writing—original draft preparation, R., R.A. and A.F.M.; writing—review and editing, R., R.A., A.F.M. and A.R.P.; visualization, R., R.A., A.F.M.; supervision, R.A., A.D.N., A.A. and A.R.P.; project administration, R., A.D.N., A.R.P.; funding acquisition, R., A.D.N., A.R.P. All authors have read and agreed to the published version of the manuscript.

Funding

This work received no external funding.

Institutional Review Board Statement

Not applicable.

Informed Consent Statement

Not applicable.

Data Availability Statement

All data has been included in the manuscript.

Acknowledgments

This research was conducted in the collaboration scheme between PT.PLN Research Institute, Research Center for Hydrodynamics Technology, OREM BRIN and Department of Mechanical Engineering, UNS.

Conflicts of Interest

The authors declare no conflict of interest.

Abbreviation

A	Johnson–Cook Yield Stress (MPa)
B	Johnson–Cook strain hardening coefficient (MPa)
C	Johnson–Cook strain rate sensitivity
CEL	Coupled Eulerian Lagrangian
c_0	Speed of sound (m/s)
D	Diameter at sensor location (mm)
D_0	Inlet diameter of water chamber (mm)
E	Young's modulus (MPa)
EOS	Equation of State
FEM	Finite Element Method
GCI	Grid Convergence Index (%)
$\hat{I}$	Nondimensional impulse
I_0	Impulse (N.s)
K	Strin hardening coefficient (MPa)
MMC	Metal Matrix Composite
m	Thermal softening exponent
$\overline{M}$	Plate mass (N)
n	Strain hardening exponent
P	Pressure (MPa)
P_m	Peak pressure (MPa)
PVC	Polyvinyl Chloride
r	Mesh refinement ratio
t	Time (ms)
USLS	Underwater Shock Loading Simulator

v_1	Initial flyer velocity (m/s)
θ	Poisson's ratio
ρ	Density (kg/m^3)
δ_max	Maximum midpoint displacement (mm)
ε	Strain
γ	Grüneisen gamma
σ	Stress (MPa)
σ_γ	Yield stress (MPa)

References

[1] Naufal, A.M., Prabowo, A.R., Muttaqie, T., et al., 2024. Characterization of Sandwich Materials — Nomex-Aramid Carbon Fiber Performances Under Mechanical Loadings: Nonlinear FE and Convergence Studies. Reviews on Advanced Materials Science. 63(1), 20230177. DOI: https://doi.org/10.1515/rams-2023-0177

[2] Wilberforce, T., El Hassan, Z., Durrant, A., et al., 2019. Overview of Ocean Power Technology. Energy. 175, 165–181. DOI: https://doi.org/10.1016/j.energy.2019.03.068

[3] Prabowoputra, D.W., Prabowo, A.R., Yaningsih, I., et al., 2023. Effect of Blade Angle and Number on the Performance of Bánki Hydro-Turbines: Assessment Using CFD and FDA Approaches. Evergreen. 10(1), 519–530. DOI: https://doi.org/10.5109/6782156

[4] Rahman, J., Aghaeidoost, V., Billah, A.M., 2024. Resilience of Coastal Bridges Under Extreme Wave-Induced Loads. Resilient Cities and Structures. 3(2), 85–100. DOI: https://doi.org/10.1016/j.rcns.2024.07.002

[5] Corigliano, P., Frisone, F., Chianese, C., et al., 2024. Fatigue Overview of Ship Structures Under Induced Wave Loads. Journal of Marine Science and Engineering. 12(9), 1608. DOI: https://doi.org/10.3390/jmse12091608

[6] Huang, W., Zhang, W., Huang, X., et al., 2017. Dynamic Response of Aluminum Corrugated Sandwich Subjected to Underwater Impulsive Loading: Experiment and Numerical Modeling. International Journal of Impact Engineering. 109, 78–91. DOI: https://doi.org/10.1016/j.ijimpeng.2017.06.002

[7] Xu, Y., Xia, D.-H., Zhang, J., et al., 2023. Mechanical Failure and Metal Degradation of Ships and Marine Structures. Metals. 13(2), 272. DOI: https://doi.org/10.3390/met13020272

[8] Nurcholis, A., Prabowo, A.R., Muhayat, N., et al., 2024. Performances of the Sandwich Panel Structures Under Fire Accident Due to Hydrogen Leaks: Consideration of Structural Design and Environment Factor Using FE Analysis. Curved and Layered Structures. 11(1), 20240005. DOI: https://doi.org/10.1515/cls-2024-0005

[9] Hanif, M.I., Adiputra, R., Prabowo, A.R., et al., 2023. Effects of the Geometrical Imperfections on the Ultimate Strength Performances: A Case Study on the Designed-Steel Stiffened Panel. Procedia Structural Integrity. 47, 125–132. DOI: https://doi.org/10.1016/j.prostr.2023.07.003

[10] Elanchezhian, C., Vijaya Ramnath, B., Ramakrishnan, G., et al., 2018. Review on Metal Matrix Composites for Marine Applications. Materials Today: Proceedings. 5(1), 1211–1218. DOI: https://doi.org/10.1016/j.matpr.2017.11.203

[11] Islami, D.P., Muzaqih, A.F., Adiputra, R., et al., 2024. Structural Design Parameters of Laminated Composites for Marine Applications: Milestone Study and Extended Review on Current Technology and Engineering. Results in Engineering. 24, 103195. DOI: https://doi.org/10.1016/j.rineng.2024.103195

[12] Alqwasmi, N., Tarlochan, F., Alkhatib, S.E., 2020. Study of Mild Steel Sandwich Structure Energy Absorption Performance Subjected to Localized Impulsive Loading. Materials. 13(3), 670. DOI: https://doi.org/10.3390/ma13030670

[13] Zhang, B., Tao, J., Cui, J., et al., 2024. Energy Absorption Characteristics of Composite Material with Fiber–Foam Metal Sandwich Structure Subjected to Gas Explosion. Materials. 17(7), 1596. DOI: https://doi.org/10.3390/ma17071596

[14] Banhart, D., Monir, S., Durieux, O., et al., 2024. A Review of Experimental and Numerical Methodologies for Impact Testing of Composite Materials. Sensing Technology. 2(1), 2304886. DOI: https://doi.org/10.1080/28361466.2024.2304886

[15] Sholikhah, M., Ridwan, R., Prabowo, A.R., et al., 2024. Strength Assessment of Stiffened-Panel Structures against Buckling Loads: FE Benchmarking and Analysis. Civil Engineering Journal. 10(4), 1034–1050. DOI: https://doi.org/10.28991/CEJ-2024-010-04-03

[16] Marx, J., Rabiei, A., 2021. Tensile Properties of Composite Metal Foam and Composite Metal Foam Core Sandwich Panels. Journal of Sandwich Structures & Materials. 23(8), 3773–3793. DOI: https://doi.org/10.1177/1099636220942880

[17] Zhao, H., Elnasri, I., Girard, Y., 2007. Perforation of Aluminium Foam Core Sandwich Panels Under Impact Loading—An Experimental Study. International Journal of Impact Engineering. 34(7), 1246–1257. DOI: https://doi.org/10.1016/j.ijimpeng.2006.06.011

[18] Latour, M., D'Aniello, M., Babcsan, N., et al., 2022. Bending Response of Sandwich Panels with Steel Skins and Aluminium Foam Core. Steel Construction. 15(2), 73–80. DOI: https://doi.org/10.1002/stco.202100044

[19] Styles, M., Compston, P., Kalyanasundaram, S., 2007. The Effect of Core Thickness on the Flexural Behaviour of Aluminium Foam Sandwich Structures. Composite Structures. 80(4), 532–538. DOI: https://doi.org/10.1016/j.compstruct.2006.07.002

[20] Ren, P., Zhou, J., Tian, A., et al., 2018. Experimental Investigation on Dynamic Failure of Carbon/Epoxy Laminates Under Underwater Impulsive Loading. Marine Structures. 59, 285–300. DOI: https://doi.org/10.1016/j.marstruc.2018.02.004

[21] Cui, X., Zhao, L., Wang, Z., et al., 2012. Dynamic Response of Metallic Lattice Sandwich Structures to Impulsive Loading. International Journal of Impact Engineering. 43, 1–5. DOI: https://doi.org/10.1016/j.ijimpeng.2011.11.004

[22] Avachat, S., Zhou, M., 2016. Compressive Response of Sandwich Plates to Water-Based Impulsive Loading. International Journal of Impact Engineering. 93, 196–210. DOI: https://doi.org/10.1016/j.ijimpeng.2016.03.007

[23] Avachat, S., Qu, T., Zhou, M., 2018. Geometry and Size Effects in Response of Composite Structures Subjected to Water-Based Impulsive Loading. In: Gopalakrishnan, S., Rajapakse, Y. (Eds.). Blast Mitigation Strategies in Marine Composite and Sandwich Structures, Springer Transactions in Civil and Environmental Engineering. Springer: Singapore. pp. 443–470. DOI: https://doi.org/10.1007/978-981-10-7170-6_23

[24] Zhu, F., Zhao, L., Lu, G., et al., 2008. Structural Response and Energy Absorption of Sandwich Panels with an Aluminium Foam Core under Blast Loading. Advances in Structural Engineering. 11(5), 525–536. DOI: https://doi.org/10.1260/136943308786412005

[25] He, X., Rong, J., Xiang, D., 2017. Damage Analysis of Aluminium Foam Panel Subjected to Underwater Shock Loading. Shock and Vibration. 2017, 1–13. DOI: https://doi.org/10.1155/2017/6031414

[26] Avachat, S., Zhou, M., 2012. Effect of Facesheet Thickness on Dynamic Response of Composite Sandwich Plates to Underwater Impulsive Loading. Experimental Mechanics. 52(1), 83–93. DOI: https://doi.org/10.1007/s11340-011-9538-4

[27] Hegde, S.R., Hojjati, M., 2019. Effect of Core and Facesheet Thickness on Mechanical Property of Composite Sandwich Structures Subjected to Thermal Fatigue. International Journal of Fatigue. 127, 16–24. DOI: https://doi.org/10.1016/j.ijfatigue.2019.05.031

[28] Muzaqih, A.F., Adiputra, R., Prabowo, A.R., et al., 2025. Analysis of Ultimate Capacity of Sandwich Composite Material Against Impulse Load: A Study Case of Fluid-Structure Interaction by FE Approach. Results in Engineering. 26, 105506. DOI: https://doi.org/10.1016/j.rineng.2025.105506

[29] Avachat, S., Zhou, M., 2015. High-Speed Digital Imaging and Computational Modeling of Dynamic Failure in Composite Structures Subjected to Underwater Impulsive Loads. International Journal of Impact Engineering. 77, 147–165. DOI: https://doi.org/10.1016/j.ijimpeng.2014.11.008

[30] Taylor, G.I., 1963. The Pressure and Impulse of Submarine Explosion Waves on Plates. In: Bachelor, G.K. (Ed.). The Scientific Papers of Sir Geoffrey Ingram Taylor, volume III: Aerodynamics and the mechanics of Projectiles and Explosions. Cambridge University Press: Cambridge, UK. pp. 287–303.

[31] Swisdak, M.M., 1978. Explosion Effect and Properties: Part II—Explosion Effect in Water. Naval Surface Weapons Center: Dahlgren, VA, USA. Available from: https://semspub.epa.gov/work/01/550573.pdf

[32] Zhang, W., Cai, Z., Zhang, X., et al., 2022. Numerical Simulation Analysis on Surface Quality of Aluminum Foam Sandwich Panel in Plastic Forming. Metals. 13(1), 65. DOI: https://doi.org/10.3390/met13010065

[33] Ye, N., Sun, Z., Guo, Q., et al., 2025. Experimental Investigation Concerning the Influence of Face Sheet Thickness on the Blast Resistance of Aluminum Foam Sandwich Structures Subjected to Localized Impulsive Loading. Metals. 15(10), 1122. DOI: https://doi.org/10.3390/met15101122

[34] Crupi, V., Epasto, G., Guglielmino, E., 2011. Impact Response of Aluminum Foam Sandwiches for Light-Weight Ship Structures. Metals. 1(1), 98–112. DOI: https://doi.org/10.3390/met1010098